Dual-Functional Boron-Modification on Cobalt-Free Single-Crystal Layered Cathode for High-Voltage Lithium-Ion Batteries

Tiancheng Liu[a], Ke Fan[a], Zezhou Lin[a], Zhuojian Liang[c], Changsheng Chen[a], Guangchao Li[a], Xuyun Guo[a,b], Yanping Zhu[a], Gao Chen[a], Hao Li[a], Tai-Sing Wu[e], Yun-Liang Soo[f], Molly Meng-Jung Li[a], Ye Zhu[a], Mingxia Dong[d] and Haitao Huang[a]*.

[a] Department of Applied Physics and Research Institute for Smart Energy, The Hong Kong Polytechnic University, Hong Kong SAR, China;

[b] School of Chemistry, Centre for Research on Adaptive Nanostructures and Nanodevices (CRANN) & Advanced Materials Bio-Engineering Research Centre (AMBER), Trinity College Dublin, Dublin, Ireland;

[c] Electrochemical Energy and Interfaces Laboratory, Department of Mechanical and Automation Engineering, The Chinese University of Hong Kong, Hong Kong SAR, China;

[d] BASF Shanshan Battery Materials Co., Ltd;

[e] National Synchrotron Radiation Research Center, Hsinchu 30076, Taiwan;

[f] Department of Physics, National Tsing Hua University, Hsinchu 30013, Taiwan.
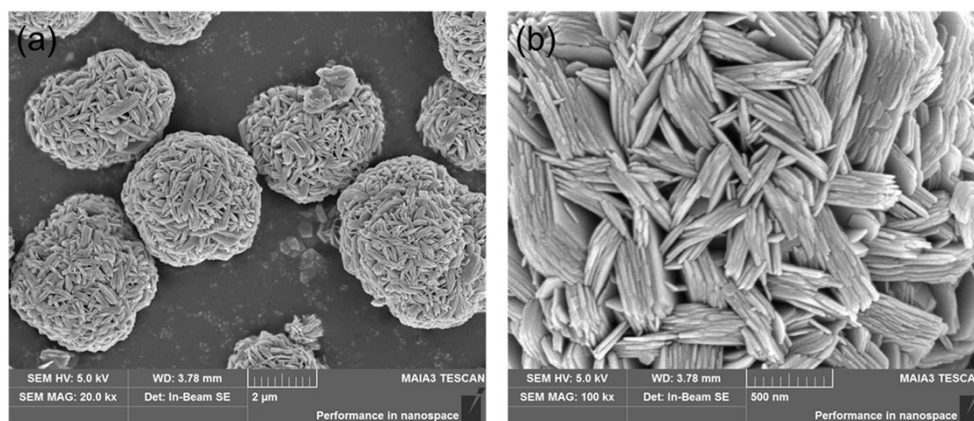
Figure S1. SEM images of $Ni_{0.75}Mn_{0.25}(OH)_2$ precursor.
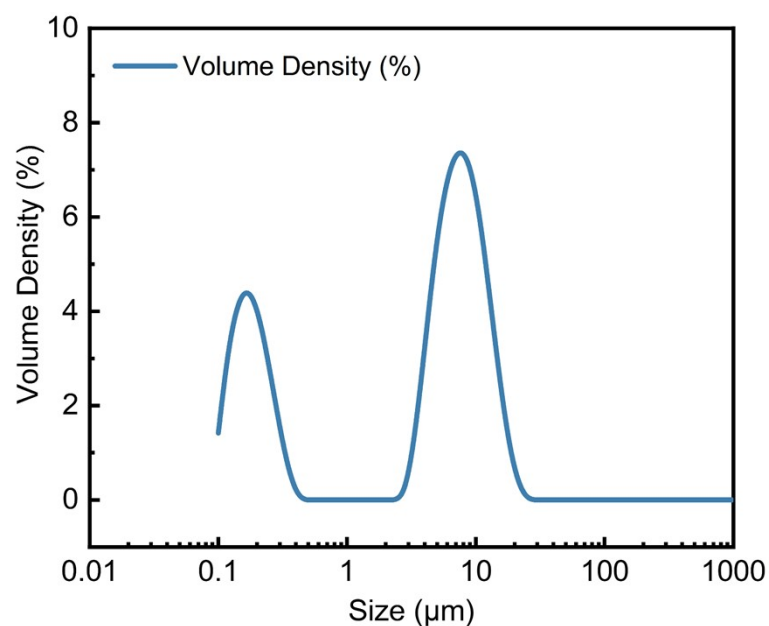
Figure S2. Particle size distribution of prepared 2#B-LNM.

The particle size determined by the particle size analyzer can be overestimated due to particle agglomeration. The SEM only looks at a very small portion of particles, while the particle size analyzer determines the average size of a relatively larger quantity of particles. Therefore, it is not surprising that the particle sizes measured by two different techniques show slight differences.
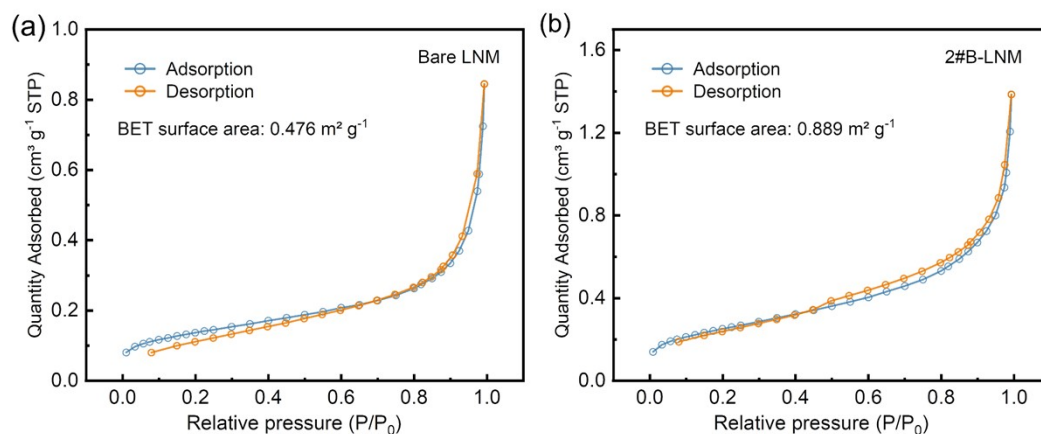
Figure S3. Isothermal N_2 adsorption/desorption curves of (a) bare LNM and (b) 2#B-

LNM.
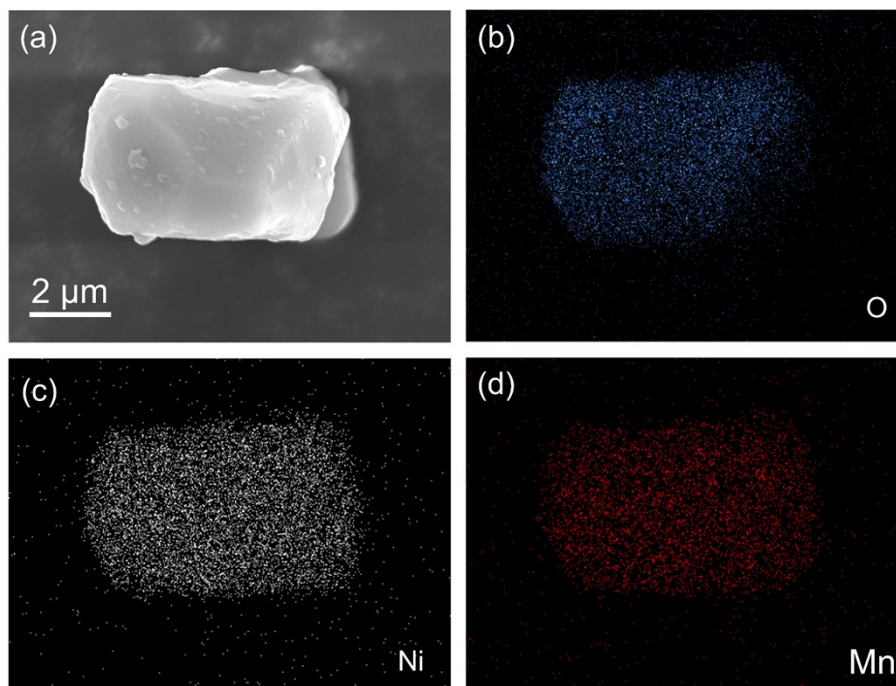
Figure S4. Elemental mapping of energy dispersive spectroscopy of synthesized bare

LNM.
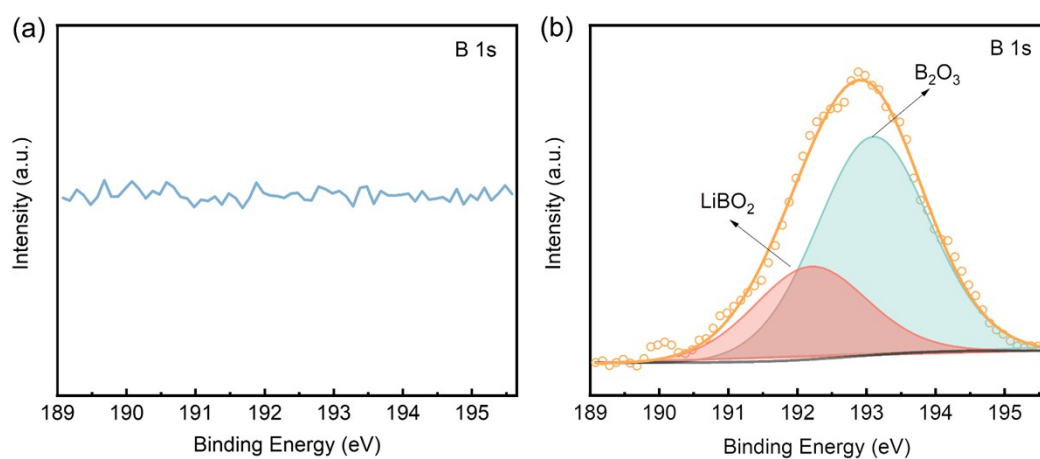
Figure S5. X-ray photoelectron spectroscopy of B 1s for (a) bare LNM and (b) 2#B-

LNM.
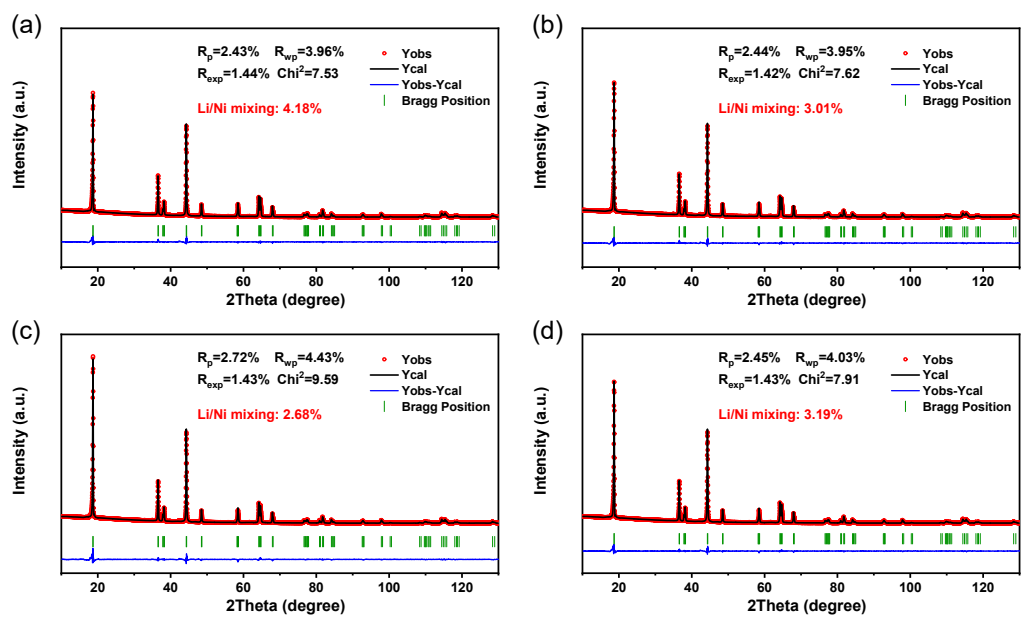
Figure S6. Conventional XRD Rietveld refinement of (a) Bare LNM, (b) 1#B-LNM, (c) 2#B-LNM, and (d) 3#B-LNM.
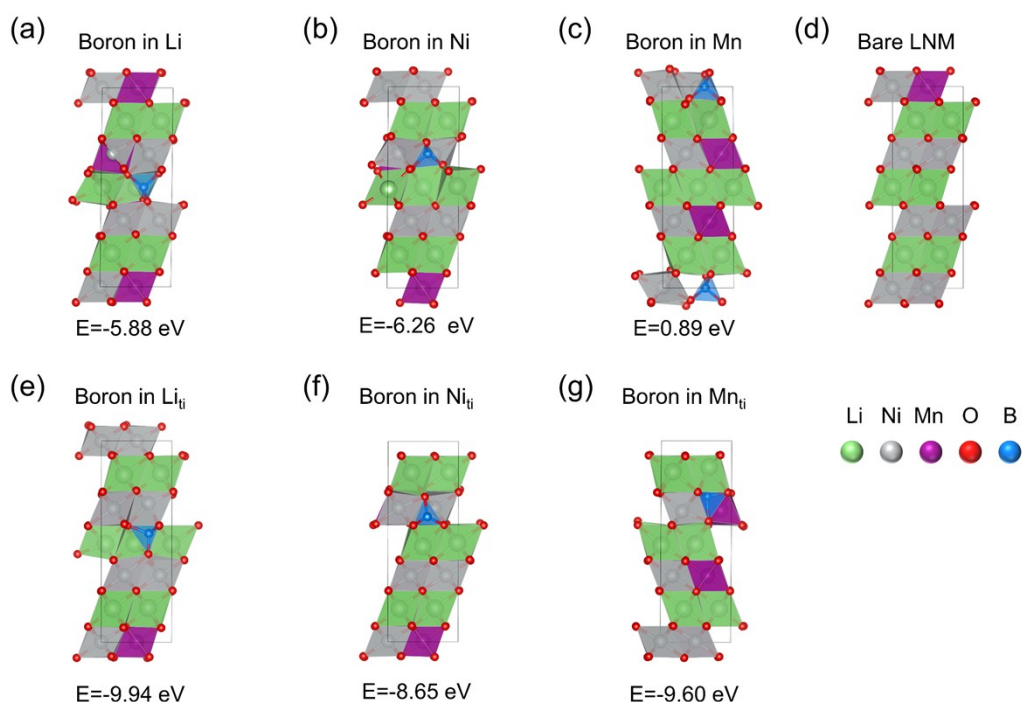
Figure S7. Atomic structures and formation energy of doping boron in various sites. Doping boron at (a) Li octahedral site, (b) Ni octahedral site, and (c) Mn octahedral sites. (d) bare LNM. Adding boron at tetrahedral interstices (denote as: ti) in (e) Li layer, (f) transition metal layer near Ni atoms, and (g) transition metal layer near Mn atoms.
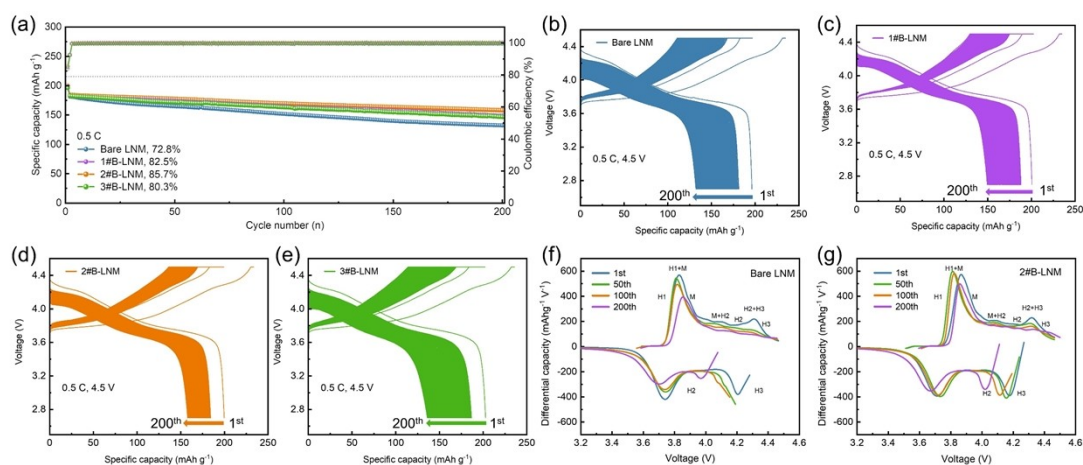
Figure S8. (a) Cycling performance (capacity retention, %) of bare LNM and different B-LNM samples at 0.5 C. Corresponding charge/discharge curves of (b) bare LNM, (c) 1#B-LNM, (d) 2#B-LNM, and (e) 3#B-LNM. dQ dV^{-1} profiles of the 1st, 50th, 100th, and 200th for (f) bare LNM and (g) 2#B-LNM.
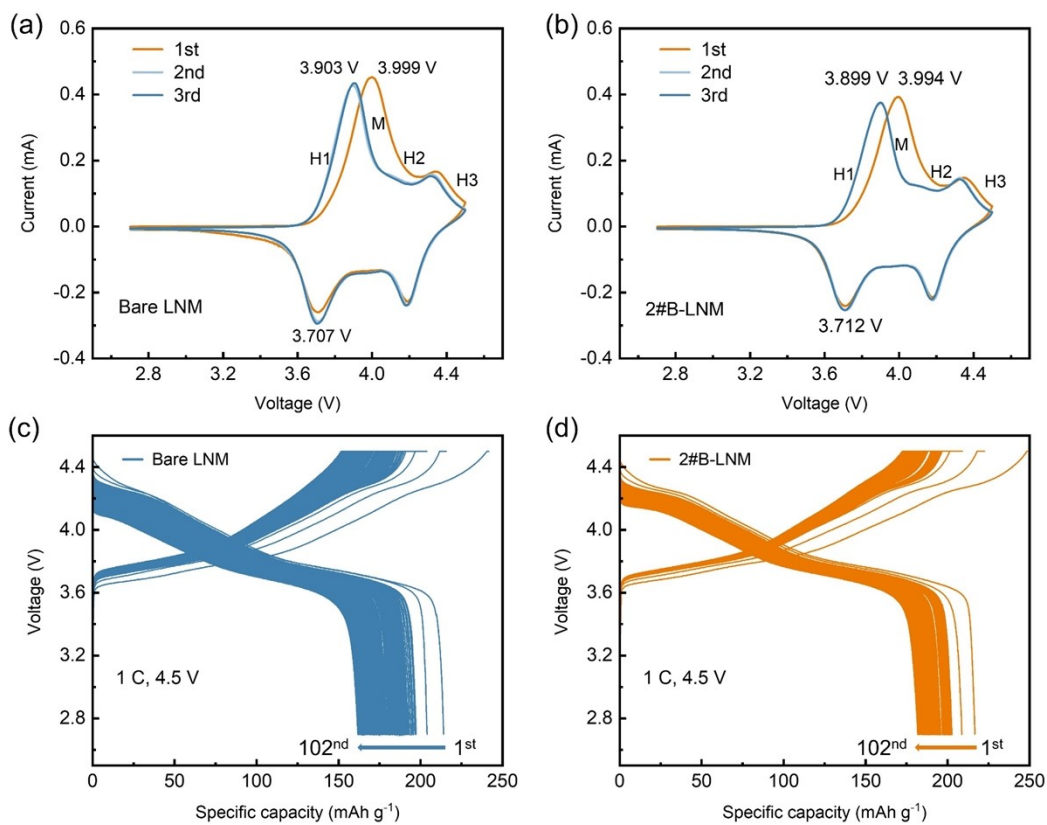
Figure S9. CV curves of (a) bare LNM and (b) 2#B-LNM for the first three cycles. Charge/discharges curves of (c) bare LNM and (d) 2#B-LNM at 60 ℃ (1C, 4.5 V). The cells were activated at 0.1 and 0.5 C for the first two cycles.
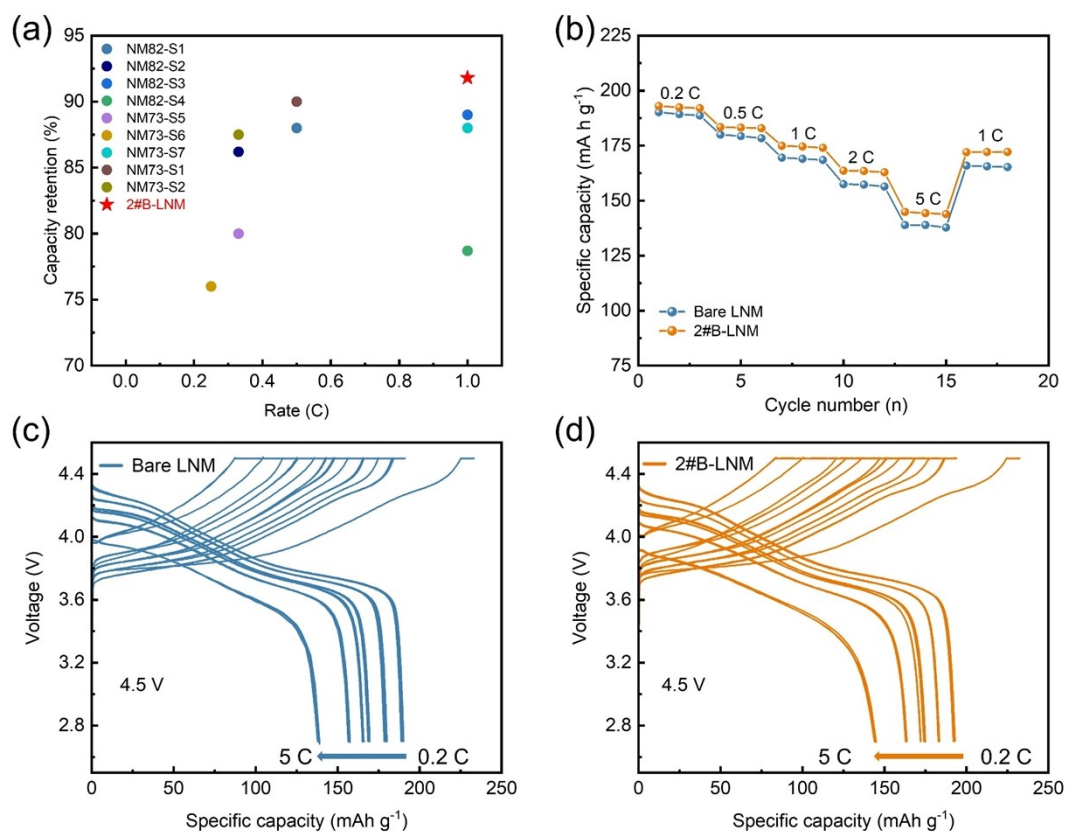
Figure S10. (a) A comparison of cycling performance with some recently reported Ni-rich Co-free layered cathodes $LiNi_xMn_{1-x}O_2$ ($0.7 \leq x \leq 0.8$) after 100 cycles. $LiNi_{0.8}Mn_{0.2}O_2$ and $LiNi_{0.7}Mn_{0.3}O_2$ are denoted as NM82 and NM73, respectively. (b) Rate performance of bare LNM and 2#B-LNM from 0.2 C to 5 C. Corresponding charge/discharge curves of (c) bare LNM and (d) 2#B-LNM.
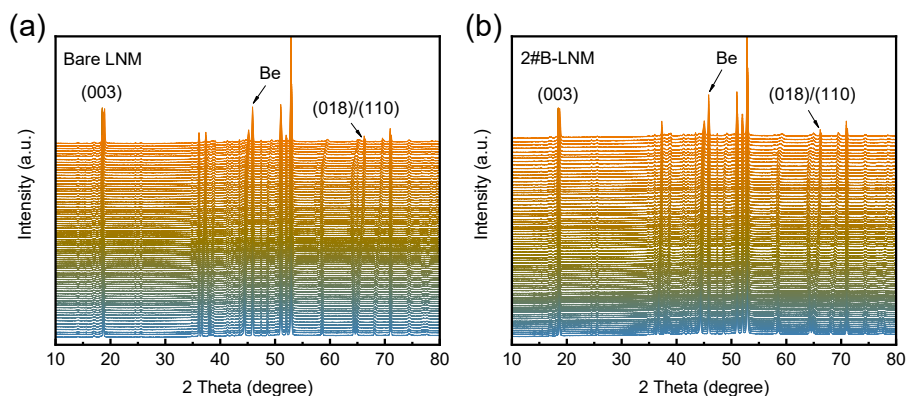
Figure S11. Full-scale in-situ XRD patterns of (a) bare LNM and (b) 2#B-LNM during the initial charge at 0.1 C until $x = 0.8$ ($Li_{1-x}Ni_{0.75}Mn_{0.25}O_2$).
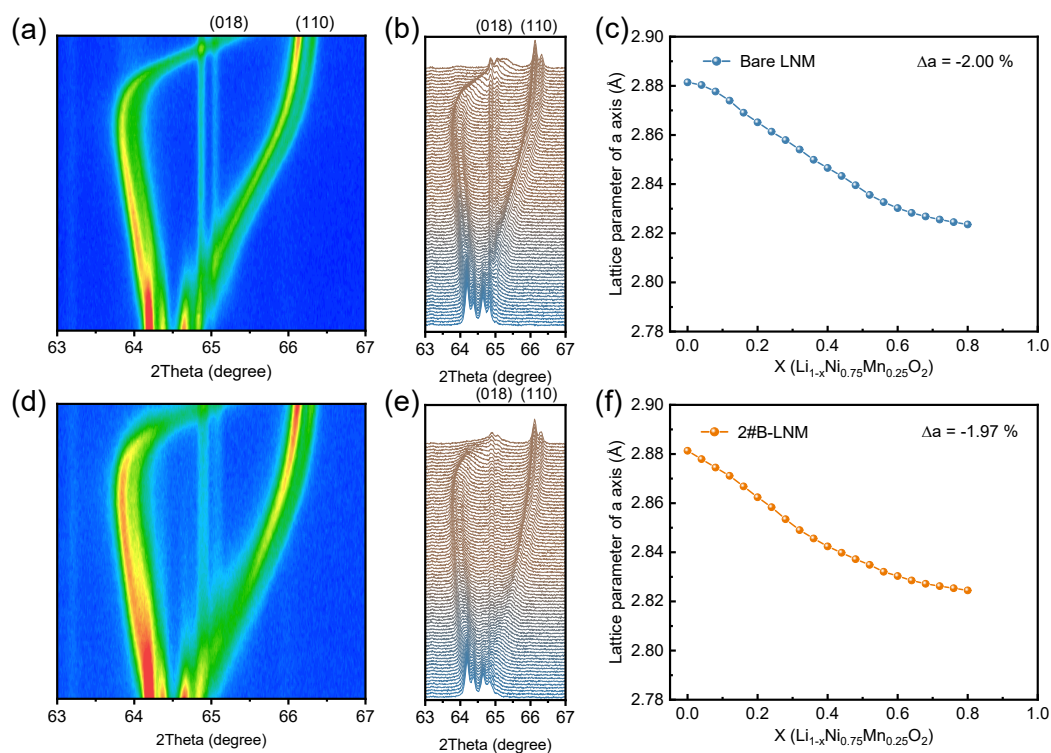
Figure S12. In situ electrochemical XRD characterization during the initial charge at 0.1 C until $x = 0.8$ ($Li_{1-x}Ni_{0.75}Mn_{0.25}O_2$): Two-dimensional contour plots of (a) bare LNM and (d) 2#B-LNM, and corresponding (018)/(110) peak patterns (b) bare LNM and (e) 2#B-LNM. The lattice parameter of the a-axis as a function of SOC: (c) bare LNM and (f) 2#B-LNM. The maximum change (%) of a-axis is indicated by Δa.
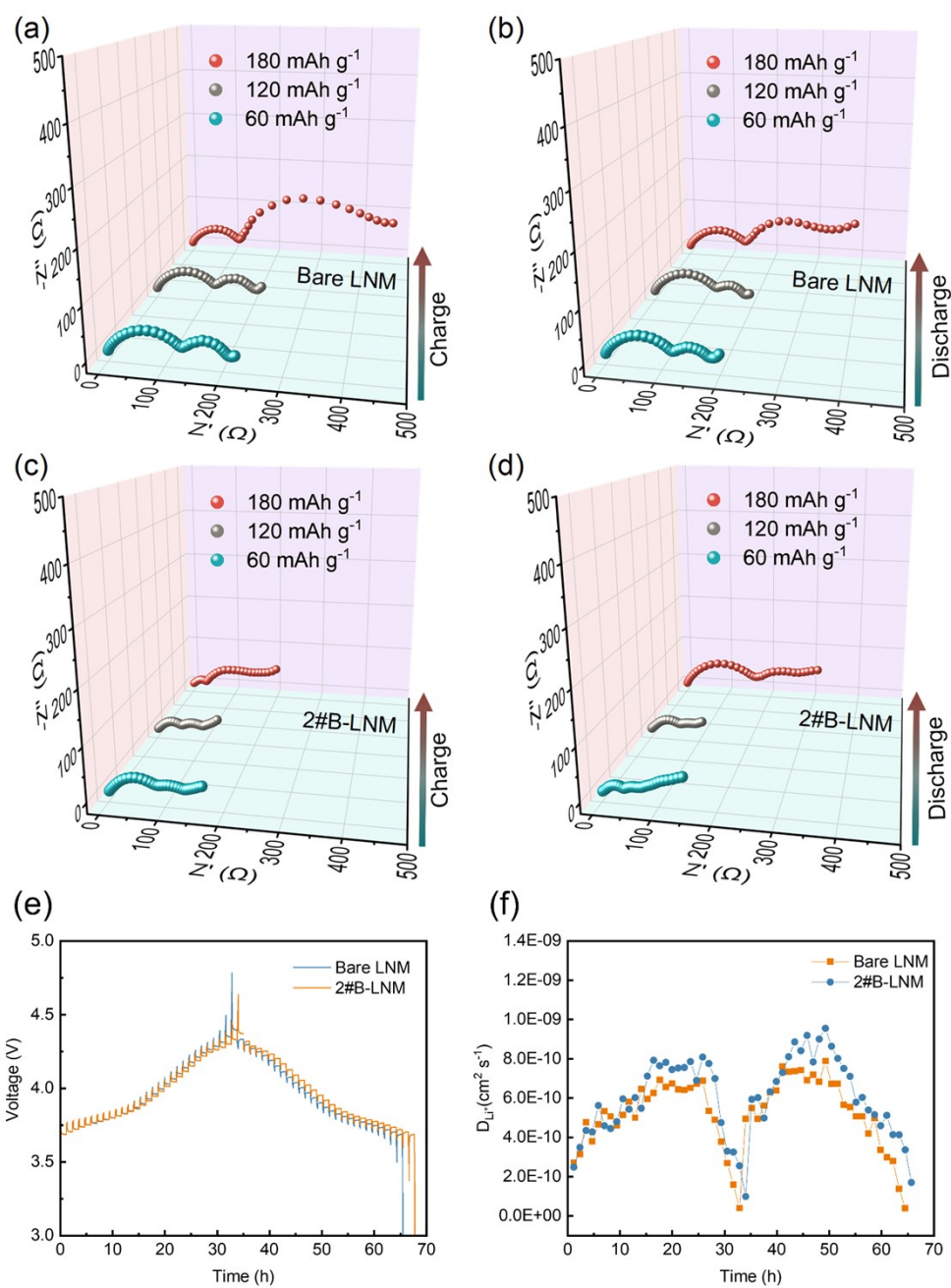
Figure S13. In situ EIS tests of (a,b) bare LNM and (c,d) 2#B-LNM during charge and discharge at 0.2 C. The cells were charged and discharged to specific capacity (60, 120, and 180 mAh g^{-1}) first, then kept idle for 1 hour before the EIS tests. (e) Charge/discharge curves of bare LNM and 2#B-LNM for GITT, and (f) corresponding lithium-ion diffusion coefficients.
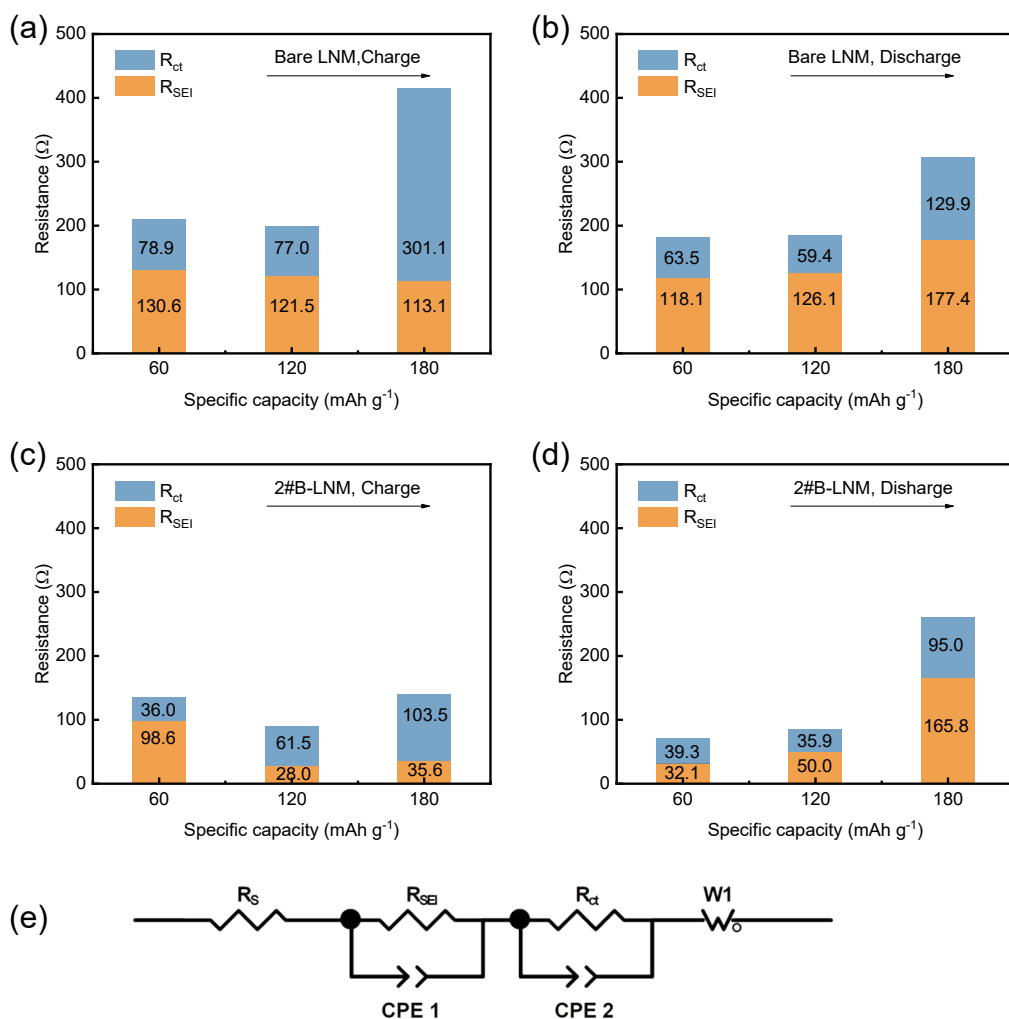
Figure S14. In situ EIS tests fitting results of (a,b) bare LNM and (c,d) 2#B-LNM during charge and discharge at 0.2 C. (e) Relevant equivalent circuit models.
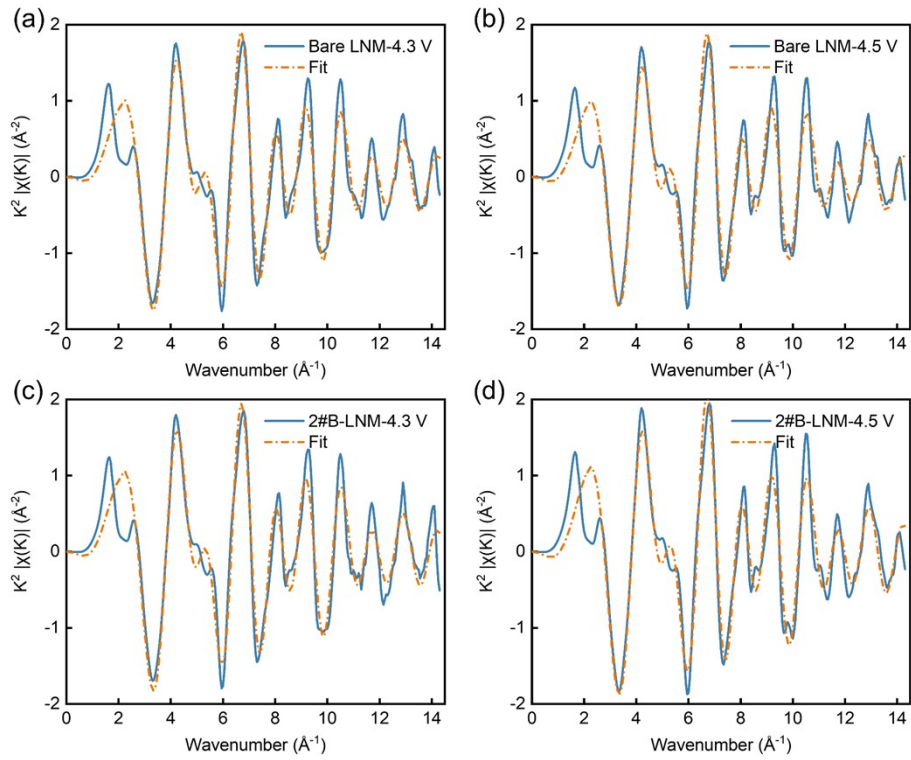
Figure S15. EXAFS fitting curves of different samples in K-space.
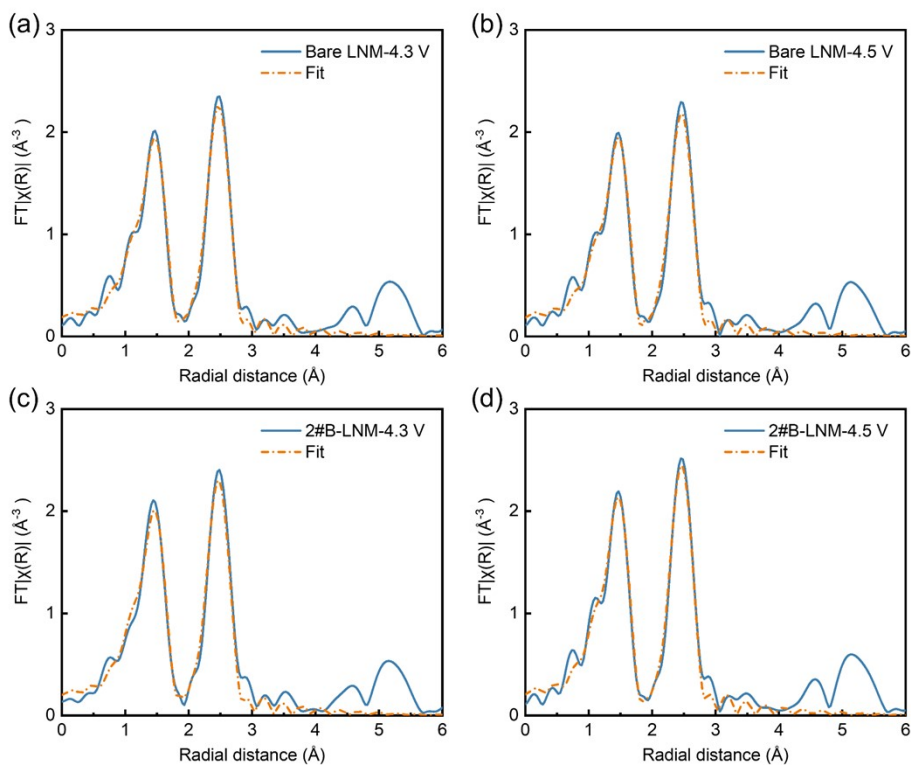
Figure S16. EXAFS fitting curves of different samples in R-space.
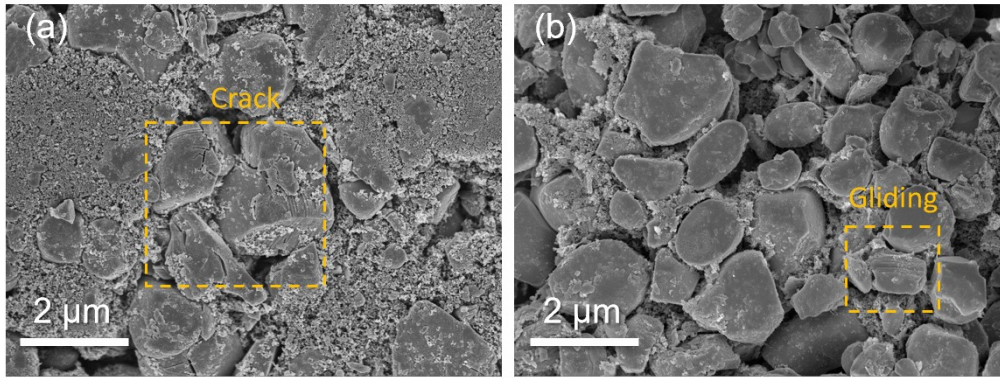
Figure S17. Surface SEM images of (a) bare LNM and (b) 2#B-LNM after 200 cycles at 1 C.
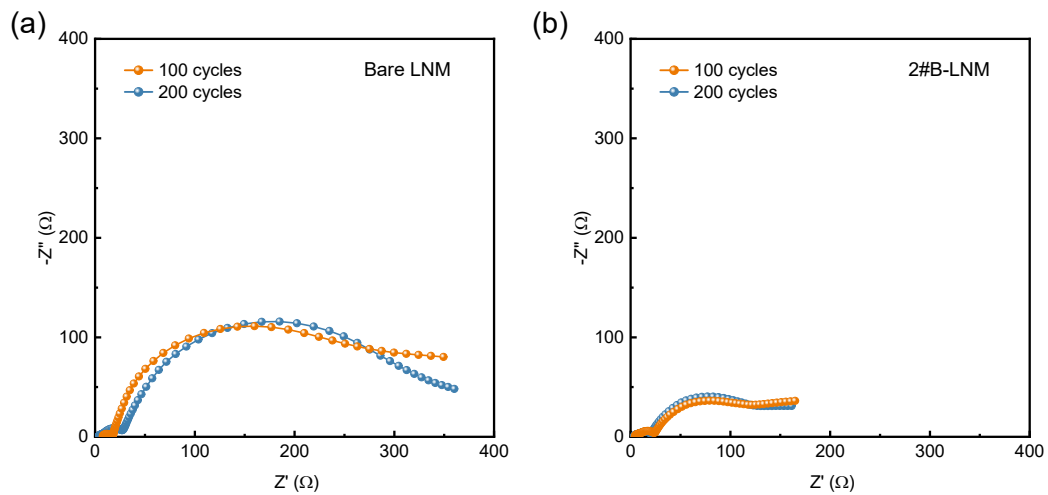
Figure S18. Nyquist plots of (a) bare LNM and (b) 2#B-LNM after 100 and 200 cycles.

Table S1. ICP-OES result of $Ni_{0.75}Mn_{0.25}(OH)_2$ precursor.

Element	Ni (mol %)	Mn (mol %)
Precursor	74.6	25.4

Table S2. Cation occupations and structural parameters based on Synchrotron XRD Rietveld refinement.

Sample	a/b-axis (Å)	c-axis (Å)	c/a	(003)/(104)	Li/Ni mixing
Bare LNM	2.8794	14.24016	4.94553	1.99	5.46%
2#B-LNM	2.8800	14.24226	4.94523	2.12	4.10%

Table S3. Cation occupations and structural parameters based on conventional XRD Rietveld refinement.

Sample	a/b-axis (Å)	c-axis (Å)	c/a	(003)/(104)	Li/Ni mixing
Bare LNM	2.8807	14.24789	4.94598	1.36	4.18%
1#B-LNM	2.8809	14.24816	4.94573	1.47	3.01%
2#B-LNM	2.8808	14.24817	4.94591	1.82	2.68%
3#B-LNM	2.8809	14.24824	4.94576	1.54	3.19%

Table S4. Lattice parameters based on DFT calculations results.

Sample	a-axis (Å)	b-axis (Å)	c-axis (Å)
Bare LNM	2.855	2.855	14.14
Boron in Li_{ti}	2.875	2.875	14.16
Boron in Ni_{ti}	2.905	2.885	14.24
Boron in Mn_{ti}	2.890	2.885	14.32

Li_{ti}: Tetrahedral interstices in Li layer;

Ni_{ti}: Tetrahedral interstices in transition metal layer near Ni;

Mn_{ti}: Tetrahedral interstices in transition metal layer near Mn.

Table S5. Comparison of cycling performance with other recently reported Ni-rich Co-free layered cathodes after 100 cycles.

Cathode	Voltage Window (V)	Current density (mA g^{-1}) (C-rate)	1st discharge capacity (mAh g^{-1})	Retention (100 cycles)	Ref
B-LiNi$_{0.75}$Mn$_{0.25}$O$_2$	**2.7-4.5**	**200 (1 C)**	**177**	**91.8%**	**This work**
LiNi$_{0.8}$Mn$_{0.2}$O$_2$	2.7-4.3	0.5	~184	~88.0%	S1[1]
LiNi$_{0.8}$Mn$_{0.2}$O$_2$	2.7-4.5	1/3	~198	86.2%	S2[2]
LiNi$_{0.8}$Mn$_{0.2}$O$_2$	2.7-4.3	1.0	~180	~89.0%	S3[3]

LiNi$_{0.8}$Mn$_{0.2}$O$_2$	2.75-4.35	1.0	~177	78.7%	S4[4]
LiNi$_{0.75}$Mn$_{0.25}$O$_2$	3.0-4.35	0.5 C/1 C	~165	95.5%	S5[5]
LiNi$_{0.7}$Mn$_{0.3}$O$_2$	2.8-4.5	1/3	~162	80.0%	S6[6]
LiNi$_{0.7}$Mn$_{0.3}$O$_2$	3.0-4.3	1/4	~163	76.0%	S7[7]
LiNi$_{0.7}$Mn$_{0.3}$O$_2$	3.0-4.3	1.0	156	88.0%	S8[8]
LiNi$_{0.7}$Mn$_{0.3}$O$_2$	2.7-4.3	0.5	~165	90.0%	S1[1]
LiNi$_{0.7}$Mn$_{0.3}$O$_2$	2.7-4.5	1/3	~183	87.5%	S2[2]

The above data are based on Co-free LiNi$_x$Mn$_{1-x}$O$_2$ ($0.7 \le x \le 0.8$) after 100 cycles except for S5 (only presents 50 cycles). ~ Data are directly collected from the figure in the corresponding references.

Table S6. Ni K-edge FT-EXAFS fitting results of Ni-O and Ni-TM.

Sample	Path	CN	R, Å	(σ^2), Å^2	ΔE_0, eV	R-factor
Bare LNM, 4.3 V	Ni-O	**4.8(2)**	1.89(1)	0.004(1)	-4.7	0.9%
	Ni-TM	4.5(1)	2.85(1)	0.003(1)	-4.5	
Bare LNM, 4.5 V	Ni-O	**4.4(1)**	1.89(1)	0.003(1)	-4.3	1.2%
	Ni-TM	4.5(2)	2.84(1)	0.003(1)	-5.1	
2#B-LNM, 4.3 V	Ni-O	**5.1(3)**	1.88(1)	0.004(1)	-4.9	1.5%
	Ni-TM	4.5(2)	2.85(1)	0.003(1)	-4.2	
2#B-LNM, 4.5 V	Ni-O	**4.9(2)**	1.89(1)	0.003(1)	-4.1	0.9%
	Ni-TM	4.6(1)	2.84(1)	0.003(1)	-5.1	

Ni K-edge FT-EXAFS fitting results of Ni-O and Ni-TM, in which CN is the average coordination number, R is the distance from the absorber atom, and σ^2 the

Debye–Waller factor. R-factor denotes the quality factor of the fitting, and ΔE_0 the energy shift from the absorption edge energy E_0.

Table S7. The fitting results of Nyquist plots for bare LNM and 2#B-LNM after the 100th and 200th cycle.

Samples	Cycle number (n)	R_{SEI} (Ω)	R_{ct} (Ω)
Bare LNM	100 cycles	4.5	195.7
	200 cycles	5.1	300.3
2#B-LNM	100 cycles	4.3	109.1
	200 cycles	4.1	114.0

References

[1] Y.K. Sun, D.J. Lee, Y.J. Lee, Z.H. Chen, S.T. Myung, Acs Appl Mater Inter, 5 (2013) 11434-11440.

[2] T.C. Liu, L. Yu, J.J. Liu, J. Lu, X.X. Bi, A. Dai, M. Li, M.F. Li, Z.X. Hu, L. Ma, D. Luo, J.X. Zheng, T.P. Wu, Y. Ren, J.G. Wen, F. Pan, K. Amine, Nature Energy, 6 (2021) 277-286.

[3] L. Zhang, L. Xiao, J. Zheng, H. Wang, H. Chen, Y. Zhu, J Electrochem Soc, 168 (2021).

[4] W. Yao, H. Zhang, S. Zhong, X. Rao, M. Zeng, Y. Fu, Journal of Inorganic Materials, 36 (2021).

[5] A. Hou, S. Xu, K. Xu, M. Zhang, D. Zhao, Ionics, 27 (2021) 4241-4248.

[6] M. Yi, W. Li, A. Manthiram, Chem Mater, 34 (2022) 629-642.

[7] D.-H. Cho, C.-H. Jo, W. Cho, Y.-J. Kim, H. Yashiro, Y.-K. Sun, S.-T. Myung, J Electrochem Soc, 161 (2014) A920-A926.

[8] D.-j. Kim, H.S. Ko, J.-w. Lee, Solid State Ionics, 278 (2015) 239-244.